Nationaal Lucht- en Ruimtevaartlaboratorium
National Aerospace Laboratory NLR

NLR-TP-2000-373

Transonic aerodynamic efficiency assessment of an optimised supersonic civil transport using CFD

J. van Muijden and A. Elsenaar

Nationaal Lucht- en Ruimtevaartlaboratorium
National Aerospace Laboratory NLR

NLR-TP-2000-373

Transonic aerodynamic efficiency assessment of an optimised supersonic civil transport using CFD

J. van Muijden and A. Elsenaar

This report is based on a presentation held at the European Congress on Computational Methods in Applied Sciences and Engineering ECCOMAS 2000, Barcelona, 11-14 September 2000.

The contents of this report may be cited on condition that full credit is given to NLR and the authors.

Division: Fluid Dynamics
Issued: July 2000
Classification of title: Unclassified

Contents

(25 pages in total)

This page is intentionally left blank.

European Congress on Computational Methods in Applied Sciences and Engineering
ECCOMAS 2000
Barcelona, 11-14 September 2000
© ECCOMAS

TRANSONIC AERODYNAMIC EFFICIENCY ASSESSMENT OF AN OPTIMISED SUPERSONIC CIVIL TRANSPORT USING CFD

J. van Muijden[*] and A. Elsenaar[†]

[*] National Aerospace Laboratory NLR
Department of Theoretical Aerodynamics and Aeroelasticity
Anthony Fokkerweg 2, 1059 CM Amsterdam, The Netherlands
e-mail: muyden@nlr.nl, web page: http://www.nlr.nl/

[†] National Aerospace Laboratory NLR
Department of Aerodynamic Engineering and Vibrations
Anthony Fokkerweg 2, 1059 CM Amsterdam, The Netherlands
e-mail: elsenaar@nlr.nl, web page: http://www.nlr.nl/

Key words: Supersonic Civil Transport, Transonic Aerodynamic Efficiency, Navier-Stokes Analysis, Comparison with Wind Tunnel Data, Reynolds Extrapolation, Sting Interference Analysis.

Abstract. *This paper describes the effort undertaken at NLR to predict the aerodynamic efficiency of a supersonic civil transport aircraft design at transonic cruise. The aircraft design consists of a wing-fuselage combination, employing leading edge deflections and one deflected trailing edge flap to meet the transonic targets. A fuselage extension to mimic the wind tunnel model sting support is taken into account.*

The aerodynamic efficiency is predicted using a multi-block structured Navier-Stokes flow analysis system. The accuracy of the computed aerodynamic coefficients is investigated in a grid refinement study. Validation of the flow solutions is based on comparison with experimental data, available from the high-speed wind tunnel DNW-HST at NLR.

Aerodynamic efficiency data at flight Reynolds number are obtained by CFD, using solution adaptive wall-normal grid spacing to adjust the boundary layer resolution. Also, the effect of the wind tunnel model sting support is investigated by additional computations on a similar configuration using the original upswept fuselage. It is shown that with present day CFD-capabilities one can predict aerodynamic efficiency for attached transonic flow around a supersonic civil transport design including deflected leading and trailing edge devices. Sufficient attention, however, has to be attributed to the quality of the computational grids.

1 INTRODUCTION

The design of a viable second generation supersonic civil transport aircraft (SCT) is a demanding task in the sense of meeting stringent aerodynamic design targets for the three relevant speed regimes: supersonic, transonic and low-speed flight. These targets are usually given in terms of aerodynamic efficiency values (target lift-to-drag ratios), while at the same time pitching moment constraints have to be met. The economic viability of a new SCT is dictated by the supersonic and transonic cruise efficiency, while the noise at take-off and fly-over at low speed determines the acceptance of a new SCT at major airports. Furthermore, environmental aspects of noise - including sonic boom - and emissions play an important role overall[1,2,3].

The reduction of supersonic aircraft drag can be sought in many ways[4]. The conventional approach, however, based on shaping the wing for optimal performance is not dependent on new or critical technologies, provided that realistic and feasible constraints are applied in the design process.

Although constrained multi-point design attempts have been performed for military aircraft and for a supersonic transport concept[5,6], meeting the ambitious targets at supersonic as well as transonic conditions using a single wing shape still poses an over-constrained optimisation problem. A more recent approach, which has confirmed the aforementioned problems using a single wing shape, circumvents the contradictory demands for the two speed regimes by a problem redefinition. First, a single point constrained optimisation is executed for the wing shape at supersonic speed. Then, variable camber is applied to this wing shape to optimise the transonic efficiency. For this purpose, deflectable spanwise leading edge segments have been defined, as well as a trailing edge flap. A similar approach can be used to tackle the low-speed design problem. Optimisation of the deflections results in promising transonic aerodynamic efficiency gains[7,8]. The design approach used in these studies is based on Euler flow analysis, using rather coarse grids as opposed to the grids used in present day analysis practice, in order to keep the optimisation process turn-around times at an acceptable level. Thus, it is of paramount importance to check the design computations on much finer grids using Navier-Stokes methods such that all drag components are addressed simultaneously and accurately.

Overviews of the European design and analysis activities related to the present in-depth transonic efficiency analysis are described by Lovell[9,10]. In the following, the attention is focussed on:

1. accuracy of flow solutions,
2. validation of computational results,
3. prediction of flight data including aerodynamic efficiency, and
4. influence of the wind tunnel model sting support.

2 CFD CALCULATIONS

2.1 Geometry handling

For the CFD calculations, the outer mold shape of the configuration is used as the starting point for volumetric grid generation. For this purpose, both fuselage geometry variants, i.e. the basic upswept fuselage as well as the extended cylindrical fuselage representing the wind tunnel model sting support, have been delivered as an ordered set of data points. The transonic wing design has been received as a set of data points, ordered as a set of consecutive airfoils. A sufficiently dense number of data points has been used to accurately represent the designed surface shape. The geometry of the wing contains the deflected leading edge segments without slots, as optimised within the design process. Also, one deflected trailing edge flap is included. As such, the airfoils have a kink in upper and lower surface at the points where the deflected portions are connected to the undeflected central part of the wing. The geometry variants, which will be denoted as wind tunnel configuration (including the fuselage extension) and flight configuration (with upswept fuselage) in the following, are shown in Figures 1 and 2. The only adjustment made to the wing shape is the addition of a minor wing tip cap to the blunt wing tip which adds one percent to the wing span. This cap is needed for the ease of grid generation around the tip.

For the purpose of wind tunnel testing, the geometry is needed to define and manufacture the wind tunnel model of scale 1:80. Since the wind tunnel model will deform during testing, an a priori finite-element based deformation computation has been performed by NLR based on the pressures at the design condition computed by Euler methods during the design process. This estimated deformation has been incorporated in the set of wing coordinates which is used to define the wind tunnel model. It is remarked here that the actual wing deformation for the wind-on design condition has been measured using the Moiré technique, which has been presented in Lovell[10]. Figure 3 depicts the transonic wing-fuselage mounted upside-down in the DNW high speed wind tunnel HST.

2.2 Grid generation

The multi-block structured flow analysis system ENFLOW[11], represented in Figure 4, has been used in the present study. Two components of this system, viz. a domain modeller to create the blocks around the configuration including the associated topological connections and a grid generator to create the grids inside blocks, have been used to create the surface and volumetric grids. The functionality of these tools include aerodynamic geometry processing, and multi-block grid generation based on algebraic and elliptic techniques[12]. The flow domain around both geometry variants has been divided into 12 blocks. A CH-type topology has been used, i.e. the grid wraps around the wing leading-edge and the fuselage, while at the wing tip the topology is simply extended towards the far-field in spanwise direction. Far-field distances have been determined on the basis of theoretical considerations[13], combined with previous transonic CFD-experience. Expressed in terms of semi-span widths, the far-fields distances used are approximately 6 semi-span widths upstream, 4 semi-span widths

downstream, 5 semi-span widths spanwise, and 10 semi-span widths above and below.

In the multi-block topology for the flight configuration special attention has been attributed to create blocks with only one face on the surface of the configuration, while the opposite face is contained in the far-field. Thus, each grid point on the surface is connected by a grid line to a grid point in the far-field. This special kind of topological definition allows for flexible adaptation of the grid in wall-normal direction for different Reynolds numbers, using a basic and efficient one-dimensional adaptation algorithm[14]. For the present study three different grids have been generated. An initial grid, denoted grid 1, refers to the first grid that has been generated specifically for analysis of the wind tunnel configuration at low Reynolds number. The features of this grid include an adjusted boundary layer grid point distribution based on the low Reynolds number, and a cell height of the first wall-normal cell in accordance with this Reynolds number. For the purpose of computing aerodynamic efficiency data at flight Reynolds number, the one-dimensional grid adaptation algorithm has been applied to grid 1, creating a thinner boundary layer with an appropriate wall-normal grid point distribution. This grid is identified as grid 2a. A third grid (grid 2b), using the same wall-normal grid point distribution as grid 2a, is generated for the flight configuration. Grid 2b is used to study the influence of the sting on the overall aerodynamics. Each grid contains approximately 3,200,000 cells. An impression of the surface grid of the flight configuration is shown in Figure 5, which is identical to the surface grid of the wing-fuselage-sting configuration from fuselage nose to wing trailing-edge. Figure 6 shows the grid in the symmetry plane, adapted to flight Reynolds number (grid 2b).

2.3 Flow solver features

The flow solver ENSOLV embedded in the ENFLOW system, see Figure 4, is capable of solving the Euler or Navier-Stokes equations on multi-block structured grids.

The flow solver provides two options for the artificial dissipation[11]. The scalar dissipation model employs non-isotropic artificial dissipation in a grid cell, which is necessary to obtain sufficiently accurate solutions on Navier-Stokes grids. Non-isotropy is obtained by applying high-aspect ratio scaling. Scalar dissipation enhances the robustness of the flow solver and can also be used when multiple Navier-Stokes directions are present within a block. The matrix dissipation model is more refined and provides a higher accuracy of the boundary layer solution, but at present its use is restricted to blocks with only one wall-normal Navier-Stokes direction. As a result, adequate skin friction drag values are obtained even on sublevels of the computational grids.

In the present study, the viscous flow computations have been performed using the thin-layer Navier-Stokes equations. The Baldwin-Lomax turbulence model with the Degani-Schiff extension for vortex-dominated flow has been used. Flow computations have been performed assuming a fully turbulent boundary layer.

3 ACCURACY OF FLOW SOLUTIONS

3.1 General considerations

The systematic assessment of numerical simulation accuracy has received major attention during the last decade[15]. This is especially significant for the prediction of aerodynamic lift, drag and pitching moment coefficients, which determine the success of any new design. In view of determining the error in the computed aerodynamic coefficients, it is not sufficient to have fine grid results only. At NLR, useful experience has been gained with the quadratic extrapolation of aerodynamic coefficients based on a sequence of three grids.

In this extrapolation approach, the finest grid is denoted with relative mesh size *h=1*. Leaving out every other grid point, a grid is obtained with relative mesh size *h=2*, and so on. Using this approach, for example on grids with relative mesh sizes *h=1*, *h=1.5* and *h=2*, an extrapolated value for vanishing relative mesh size can be obtained for any aerodynamic coefficient. If the grid dependency of aerodynamic coefficients is parameterised by

$$C(h) = C_1 + C_2\, h + C_3\, h^2, \tag{1}$$

where C_1, C_2 and C_3 denote constants, then numerical values for these constants are easily found from the coefficient values at three different relative mesh sizes *h*. This extrapolation procedure is based on the notion that the local accuracy of the numerical scheme is a mix of first- and second-order terms that introduce respectively a linear and a quadratic dependency on the relative mesh size. The validity of this approach has been investigated in the past at NLR by performing a number of computations for fixed incidence and for fixed lift, resulting in identical extrapolated values for the aerodynamic coefficients when sufficiently fine grids are used[16].

However, it is not always possible to perform computations on a range of sufficiently fine grids with relative mesh size ratios of 1, 1.5 and 2. When a computational grid with at least three levels of multi-grid is available, it is possible to use the results obtained on each of the grid levels denoted with *h=1*, *h=2* and *h=4*. Quadratic extrapolation gives an indication of the difference between directly computed coefficients on the finest grid and the expected coefficient values for vanishing relative mesh size. The reliability of the quadratic extrapolation depends on:

1. the number of grid cells in the finest grid and its sublevels,
2. the overall quality of the volumetric grids in terms of orthogonality, cell aspect ratios and stretchings, and
3. the attained convergence on each grid level.

In the present study all calculations are performed at fixed lift coefficient. Therefore, a crosscheck on the flow solutions accuracy is given by extrapolation of results obtained on grids with different wall-normal resolution (grid 1 versus grid 2a). At the same time, two different artificial dissipation models have been used, viz. matrix versus scalar dissipation. The robustness of the matrix dissipation model is hampered on grids having extremely high aspect-ratio cells, which are encountered in grids for very high Reynolds number computations. Therefore, the results presented here are mainly obtained using the non-

isotropic scalar dissipation model on grids with high boundary layer resolution (grid 2), whereas the matrix dissipation model is used to crosscheck the computational results using the grid adapted for low Reynolds number (grid 1).

Finally, it is remarked that the aerodynamic coefficients in this study have been obtained by direct integration of surface pressure and friction contributions, which is the so-called near-field approach[16].

3.2 Flow solution numerical accuracy assessment

In Table 1, an overview is presented of computed flow cases that have been used for the determination of flow solution accuracy based on grid refinement studies. All cases have been computed for fixed design lift coefficient. As an indication of convergence, all cases have been iterated until coefficient convergence and approximately three orders of magnitude residual decrease had been established. Especially useful is the first case mentioned, which allows for an independent crosscheck of the low Reynolds number results. The number of grid cells is related to the relative mesh size *h* as given in Table 2.

Table 1. Overview of computed flow cases for use in grid-refinement study.

Case	Configuration	Grid	Mach	C_L	Reynolds	Dissipation Model
1	Wing-fuselage-sting	1	0.95	0.192	7.9 million	Matrix
2	Wing-fuselage-sting	2a	0.95	0.192	7.9 million	Scalar
3	Wing-fuselage-sting	2a	0.95	0.192	198.6 million	Scalar
4	Wing-fuselage	2b	0.95	0.192	198.6 million	Scalar

Table 2. Grid density information for the SCT-configurations

Relative mesh size *h*	Grid level	Total number of grid cells	Number of surface cells	Number of wall-normal cells	Approximate number of cells in boundary layer
8	1	6,250	360	11	6
4	2	50,000	1,440	22	11
2	3	400,000	5,760	44	22
1	4	3,200,000	23,040	88	44

Figure 7 shows the grid dependency of the drag coefficients of cases 1 and 2, computed on grids with two different wall-normal grid point distributions and using two different dissipation models. As expected, the scalar dissipation model results in a much higher grid dependency of the computed drag than the matrix dissipation model. However, results on the finest grid levels *(h=1)* are nearly identical despite these differences, showing that the increased near-wall resolution of grid 2a compensates for the disadvantages of the scalar dissipation model. Using quadratic extrapolation, a nearly identical drag value for vanishing relative mesh size is found (within 0.25 drag counts), despite the large differences in drag on coarser grid levels. In view of industrial requirements for drag prediction (accuracy of 1 drag

count), the results show that these requirements can be met using common grid sizes combined with quadratic extrapolation.

In Figure 8, the same crosscheck is depicted for the pitching moment coefficient. Here, it is found that fine grid values differ significantly while grid dependencies have similar magnitude for both dissipation models, although the matrix dissipation model results in a more linear behaviour with relative mesh size *h*. Using quadratic extrapolation, slightly different pitching moment coefficient values for vanishing relative mesh size are found. Finer grids may be required to further reduce the pitching moment value uncertainty.

For these computations at fixed lift coefficient, the angle-of-attack can also be checked as shown in Figure 9. In the same fashion as for the drag coefficient, identical values for vanishing relative mesh size are obtained.

Thus, the consistency of the quadratic extrapolation procedure is once again verified. It is also shown that pitching moment coefficient accuracy is the most prominent factor for the determination of the number of grid cells in the fine grid *(h=1)*. This is directly related to the sensitivity of pitching moment with respect to small pressure changes at large distances from the moment point.

Finally, quadratic extrapolations are shown for cases 3 and 4 at flight Reynolds number. Identical wall-normal grid point distributions are used, adjusted for the high Reynolds number. Now the extrapolations cannot be formally cross-checked with a second set of computations. Figure 10 gives the drag as a function of relative mesh size for the wind tunnel configuration (case 3). As can be observed, the dependency on relative mesh size is somewhat larger than for the low Reynolds number, showing that the wall-normal resolution in the boundary layer for this higher Reynolds number could be improved. However, since the drag decreases towards vanishing relative mesh size, the fine grid *(h=1)* value provides a conservative drag estimate. The pitching moment extrapolation is shown in Figure 11. Here, grid dependency is comparable to the low Reynolds number case 2, leading to an even more nose-down extrapolated pitching moment value. Figure 12 depicts the angle-of-attack as a function of the relative mesh size, showing that the extrapolated value is about 0.1 degrees lower than the fine grid result, as has also been found for case 2.

Figures 13 to 15 show the grid dependency of drag, pitching moment and angle-of-attack for case 4, containing the upswept fuselage. The trends are similar to those of case 3. The difference in drag between case 3 and case 4 is of equal magnitude on the fine grid level as for vanishing relative mesh size. Similar observations can be made for the pitching moment coefficient and angle-of-attack. Thus, for the study of the upswept fuselage versus the extended fuselage to mimic the wind tunnel model sting support, coefficients can be compared on the fine grid directly.

4 THE VALIDATION EXPERIMENT

Wind tunnel tests have been carried out for two reasons: to allow a direct evaluation of the design and to validate the CFD method. The layout of the wind tunnel model and details of the experimental program have been finalised after intensive discussions. The wind tunnel model has been designed and manufactured by NLR. For practical reasons three different wings (for respectively the supersonic, transonic and low speed design condition) have been manufactured. These three wings with different leading and trailing edge deflections are mounted on the same fuselage. Each wing has three pressure sections (at 29, 52 and 71 percent half span respectively) with 90 pressure holes in total. The supersonic tests have been performed in the 1.1 by 1.2 m^2 supersonic blow down tunnel SST, whereas low speed and transonic tests have been made in the 1.6 by 2.0 m^2 pressurised transonic tunnel HST. In the latter case the tests were made at about 2 bar static pressure resulting in a Reynolds number of about 18 million based on root chord. Both tunnels are operated by the DNW organisation. Only the transonic tests will be described in more detail here.

The model is 0.936 m long with a span of 0.525 m and a wing reference area of 0.1371 m^2. This size has been determined mainly by the supersonic configuration (in view of the start- and stopping loads in the blow-down facility). The wing of a supersonic transport is relatively thin, therefore very difficult to manufacture and subject to wing deformation, either in the machining process or under aerodynamic load. For that reason it has been decided to give the wing a pre-deformation such that in the transonic design condition the required wing shape is recovered. Moreover, the actual deformation has been measured in the wind tunnel using the Moiré technique (see Figure 3 showing the white painted lower surface of the right wing half, as required for this type of measurements). These measurements roughly confirmed the pre-test estimated wing deformation: almost zero up to 50 percent of the half span and increasing to about one degree at the outer wing tip. The shape of the unloaded wing has also been measured on a precision measuring machine. From these measurements it could be concluded that variations in the wing shape (local incidence setting) for the outboard wing (between 50 percent of the half span and the tip) are of the order of 0.2 degrees at most. Inboard of the 50 percent half span the wing can be considered as undeformed. This was also confirmed by pressure measurements (a number of pressure holes was duplicated on both wing halves to establish by comparison possible differences between the port and the starboard wing halves). When these geometry variations are averaged over the wing, an incidence variation of the order of 0.05 degrees (relative to the ideal wing setting) is to be expected, a very acceptable value in view of the thin outer wing and the complexity of the model including its instrumentation.

Mounting the model in the wind tunnel necessitated a deformation of the rear fuselage: the cylindrical central section has been continued till the end of the model. A slender straight sting has been used, to minimise a possible upstream effect of the model support. Since some upstream effect is always present, the drag and local pressures have been corrected on the basis of long static pipe measurements as part of the normal calibration procedure for model supports. The base and cavity pressures have been measured and the drag has been corrected

on the basis of these measured values (relative to the free stream static pressure). The model is relatively small for the HST and for that reason wall interference effects can be excluded as was confirmed by wall pressure measurements. The force measurements were made with a high accuracy balance with an estimated accuracy in the measured aerodynamic coefficients of 0.002 in lift, 0.0002 in drag and 0.0003 in pitching moment. Upright and inverted model tests indicated a reproduction well within this accuracy after the application of the appropriate tunnel 'upwash' correction.

Artificial transition fixation has been used to assure (almost) full turbulent boundary layer flow. A thin band of carborundum has been wrapped around the nose of the fuselage. Judging from the pressure distributions, it can be anticipated that the boundary layer will be turbulent after the pressure peaks generated at the kink of the deflected leading edge. However, there is a real risk that if the flow on the deflected leading edge is laminar, laminar boundary layer separation might occur at the kink location, resulting in a bubble with a possible adverse effect on drag. For that reason a transition strip on the upper and lower deflected leading edge has been applied over the full span. This strip was at a constant (perpendicular) distance of 3 mm from the leading edge. All transition strips have been verified using acenaphtene.

Force and pressure measurements have been performed separately. The force measurements have been derived from a continuous sweep, whereas the pressure measurements have been obtained in 'pitch-pause'.

By and large, all reasonable precautions have been taken to assure a set of reliable experimental data that can be used with confidence to validate the design and CFD methods.

5 VALIDATION OF FLOW SOLUTIONS

Validation of flow solutions is accomplished by comparison with experimental data available from the DNW high-speed wind tunnel HST. First of all, pressure distributions at selected span stations for the design condition are shown in Figure 16, comprising the medium and fine grid level results and the wind tunnel data. As can be observed, the medium grid level already yields acceptable pressure distributions, although details near shock waves, especially shock resolution, are improved on the fine grid. Also, shock waves on the fine grid are found to be slightly aft of the experimental shock position, which is not uncommon in CFD-results based on the Baldwin-Lomax turbulence model. However, the overall comparison with the experimental pressure distribution is excellent.

In order to further compare the details of the flow at the design condition, a comparison is made between the limiting streamlines from the computed flow solution and the oil flow pattern from the wind tunnel, see Figures 17 and 18. Identical patterns are found, including the separation near the wing tip aft of the kink. However, the calculated separation appears to be somewhat smaller than the one in the experiment, which could be caused by the assumption of fully turbulent boundary layers in the CFD-calculations.

A comparison between computed and experimental aerodynamic coefficients completes the picture. For this purpose, two additional computations at a higher and lower lift value have been added. Fine grid results only have been used here for comparison. Figure 19 shows

the comparison of the computed and measured lift curve. A good agreement is found, although a mismatch can be observed that is lift dependent. Keeping in mind that the wind tunnel model has been pre-deformed to reach the design shape for wind-on conditions at the design lift, the higher loads at increasing incidence lead to larger wing deformations. This results in increasingly lower lift values than predicted on the design shape using CFD. The comparison between computed and measured pitching moment coefficients versus lift is given in Figure 20. Once again, a good comparison is found, showing small mismatches increasing with lift. In view of the shock wave position that is found to be slightly aft of the experimental shock position, the calculated pitching moment values are expected to differ from the measured values. The lift-dependency of the mismatch has to be attributed to the model deformation.

Based on the three computed flow conditions and the assumption that the drag polar, for fixed Mach and Reynolds number, can be approximated by a quadratic polynomial in the form

$$C_D - C_{D0} = (C_L - C_{L0})^2 / (\pi A e), \tag{2}$$

with A the wing aspect ratio, e the Oswald factor and C_{D0} and C_{L0} denoting constants, a solution of the three unknowns in (2) is obtained. Figure 21 shows the measured drag polar and the computed data points, as well as the estimated drag polar. The overall comparison is good, having a more or less constant drag difference in the region of interest around the design lift coefficient. At the design condition, the computed drag is approximately 4 drag counts below the measured value.

6 PREDICTION OF FLIGHT AERODYNAMICS

6.1 Calculated Reynolds number effects and aerodynamic efficiencies

The relatively small wind tunnel model restricts the maximum attainable Reynolds number during transonic testing to rather small values. A factor of more than 20 on the Reynolds number is needed to verify the aerodynamic efficiency at flight conditions. At present, this can only be achieved using CFD.

Identical flow conditions have been computed at the flight Reynolds number to determine the aerodynamic efficiency at the design point, and to estimate the drag polar. This has been performed for the wind tunnel configuration as well as for the flight configuration that resembles the real aircraft to a much higher degree. The results of this procedure are given in Figure 22, which includes the estimated low Reynolds number polar for comparison. As expected, the drag at high Reynolds number is much lower, basically due to the reduced friction drag contribution. Also shown is the small increase in drag when the fuselage extension, resembling the wind tunnel model sting support, is replaced by the upswept fuselage shape. Details of the sting effect will be addressed in the next section.

In terms of aerodynamic efficiency, the increase in Reynolds number naturally leads to a higher value. Figure 23 shows the behaviour of the aerodynamic efficiency *L/D* versus lift

coefficient, based on the estimated drag polars. An increase of the aerodynamic efficiency at the design point of about 20 percent is found for the wind tunnel configuration at flight Reynolds number, whereas the maximum value for *L/D* changes with about the same percentage. The aerodynamic efficiency of the flight configuration is found to be 15.99 at the design point, against a value of 16.87 for the wind tunnel configuration at flight Reynolds number. In view of the transonic design target, which aims at a value of 15, the present design fulfills the aerodynamic efficiency needs for a second generation SCT. Finally, the Reynolds number effect on angle-of-attack is shown in Figure 24, whereas the Reynolds number effect on pitching moment is depicted in Figure 25. It is observed that the Reynolds number effects are lift-dependent. Since the shock position has been found to be very sensitive to parameter changes (see Figure 26), the Reynolds number effect on the displacement thickness and thus on shock position explains the lift-dependency.

6.2 Sting interference effects

It has been found that the flight configuration leads to a higher drag than the wind tunnel configuration at identical flow conditions. The most prominent factor contributing to this drag change obviously is the replacement of the fuselage extension, which mimics the wind tunnel model sting support, by the upswept fuselage shape. The effect of this change on the pressure distribution is shown in Figure 27. A rather significant change in shock position is found. Although the sensitivity of shock position with small parameter changes has been confirmed by the wind tunnel experiments as depicted in Figure 26, the computed shock position changes cannot be explained in terms of changes in angle-of-attack. Therefore, a careful examination of the after-body shape differences is required. As is obvious from the delivered geometry definitions, the wind tunnel configuration has been given a fuselage with a constant cross-section aft of the nose part, which is required to allow model mounting of the relatively small model on the sting having sufficient margins in the fuselage material to withstand the expected structural loads. Also, the instrumentation of the wind tunnel model requires this internal volume.

The upswept fuselage, however, differs from the wind tunnel fuselage not only aft of the wing trailing edge, but also upstream starting at approximately one wing tip chord before the wing trailing edge. This reduction in local fuselage diameter leads to accelerating flow on the wing. This acceleration can be understood bearing in mind that the local flow is supersonic ahead of the shock. As a result, the shock wave is found somewhat further downstream than on the wind tunnel configuration, see Figure 28. The larger extent of the supersonic region at the design lift coefficient explains the somewhat smaller angle-of-attack for the flight configuration at identical lift coefficient, see Figures 12 and 15.

Thus, it can be concluded that differences between wind tunnel and flight configuration cannot be fully attributed to the presence of the sting, but are partially induced by geometrical differences of the afterbody shape ahead of the sting as depicted in Figure 28.

7 CONCLUDING REMARKS

A supersonic civil transport design for transonic cruise conditions has been successfully analysed using the NLR ENFLOW multi-block structured flow analysis system. Two geometrical variants have been used, viz. a wind tunnel configuration consisting of a wing-fuselage-sting combination, and a flight configuration wing-fuselage combination with an upswept fuselage afterbody shape. Efficient grid generation for two largely different Reynolds numbers has been accomplished using a basic, one-dimensional grid adaptation procedure. It has been shown that the accuracy of computed aerodynamic coefficients can be checked by a quadratic extrapolation procedure towards vanishing relative mesh size, using the results as obtained on three grid levels. Validation of the flow solutions is performed by comparison with wind tunnel measurements. For the case considered, an excellent agreement is found in the pressure distributions, while good overall agreement is shown in the comparison of aerodynamic coefficients. Predictions of aerodynamic efficiency have been given at flight Reynolds number, showing that the transonic wing design meets the design target.

It is concluded that realistic aerodynamic efficiency predictions for attached transonic flow can be obtained with present day Navier-Stokes CFD capabilities, provided that sufficient attention is attributed to the quality of the computational grids.

ACKNOWLEDGEMENTS

The cooperation with all partners within the European project EUROSUP[10] and the support from the Commission of the European Union are gratefully acknowledged.

REFERENCES

[1] C. Michaut, " The Second Generation Supersonic Transport Aircraft Challenges", *ICAS-94-1.2.3,* (1994).

[2] M. Pacull and P.K. Green, "European Second Generation Supersonic Transport", *Proceedings of the 7th European Aerospace Conference EAC '94, Toulouse*, (1994).

[3] T. Iwaki and M. Sunakawa, "Overviews of Japanese Study Activities for the Second Generation SST", *ICAS-94-1.2.1,* (1994).

[4] D. Bushnell, "Supersonic Aircraft Drag Reduction", *AIAA 90-1596*, (1990).

[5] D.A. Lovell and J.J. Doherty, "Aerodynamic Design of Aerofoils and Wings Using a Constrained Optimisation Method", *ICAS-94-2.1.2*, (1994).

[6] J.J. Doherty and N.T. Parker, "Dual-Point Design of a Supersonic Transport Wing Using a Constrained Optimisation Method, *Proceeding of the 7th European Aerospace Conference EAC '94, Toulouse*, (1994).

[7] R. Grenon, "Numerical Optimization in Aerodynamic Design with Application to a Supersonic Transonic Transport Aircraft", *ONERA TP 1998-16*, (1998).

[8] S.C. Rolston, J.J. Doherty, T.P. Evans, R. Grenon and M.A. Averardo, "Constrained Aerodynamic Optimisation of a Supersonic Transport Wing: a European Collaborative Study", *AIAA-98-2516*, (1998).

[9] D.A. Lovell, "Reduction of Wave and Lift-Dependent Drag for Supersonic Transport Aircraft", *ICAS-98-2,1,1*, (1998).

[10] D.A. Lovell, "European Research to Reduce Drag for Supersonic Transport Aircraft", *AIAA-99-3100*, (1999).

[11] J.C. Kok, J.W. Boerstoel, A. Kassies and S.P. Spekreijse, "A Robust Multi-Block Navier-Stokes Flow Solver for Industrial Applications", *Proceedings of the 3rd ECCOMAS Conference, Paris*, (1996), also NLR TP 96323, (1996).

[12] S.P. Spekreijse, "Elliptic Generation Systems", In: *Handbook of Grid Generation*, CRC Press, (1999).

[13] J. van der Vooren, "On the Proper Shape of a Finite Computational Domain for Potential Flow Methods", *Appendix C in: Accuracy Study of Transonic Flow Computations for Three-Dimensional Wings*, GARTEUR AD(AG-05), Volume I Text, GARTEUR TP-030, (1988).

[14] R. Hagmeijer, "Grid Generation in Turbulent Boundary Layer Using Theoretical Velocity Distribution", *NLR-TR-99137*, (1999).

[15] AIAA Standards Department, "Guide for the Verification and Validation of Computational Fluid Dynamics Simulations", *AIAA G-077-1998*, (1998).

[16] B. Oskam and J.W. Slooff, "Recent Advances in Computational Aerodynamics at NLR", *AIAA 98-0138*, (1998).

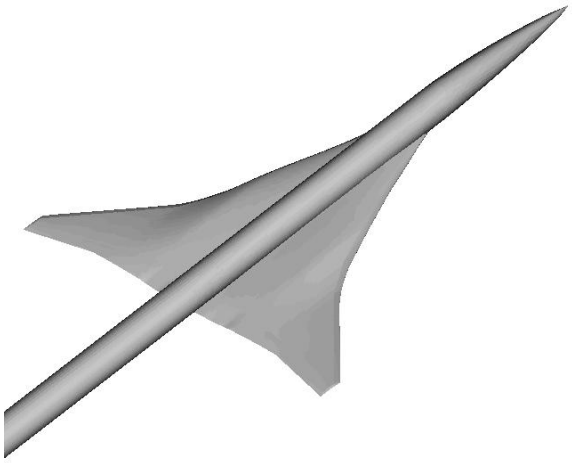

Figure 1: Wind tunnel configuration

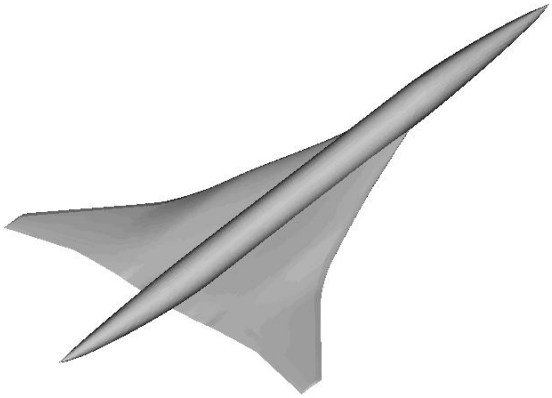

Figure 2: Flight configuration

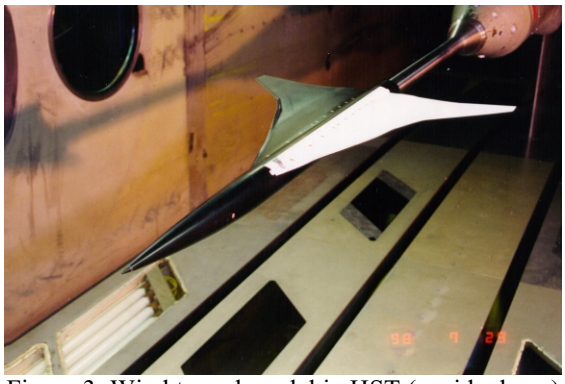

Figure 3: Wind tunnel model in HST (upside down)

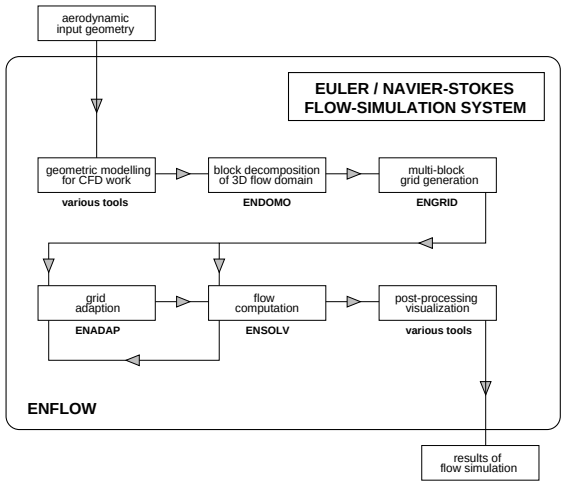

Figure 4: CFD-system based on multi-block structured grids

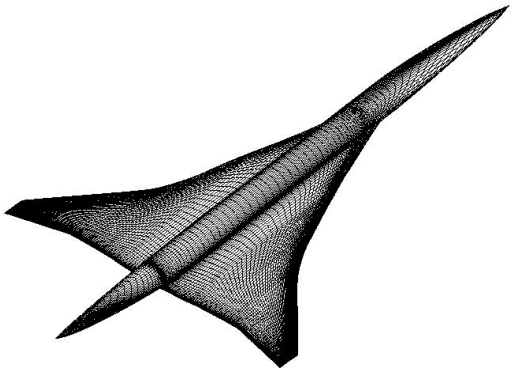

Figure 5: Impression of surface grid

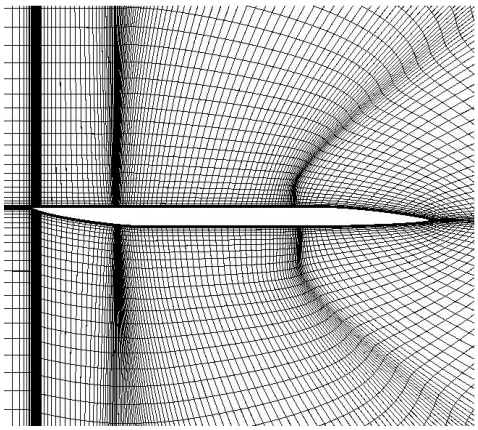

Figure 6: Grid in the symmetry plane adapted in wall-normal direction for flight Reynolds number

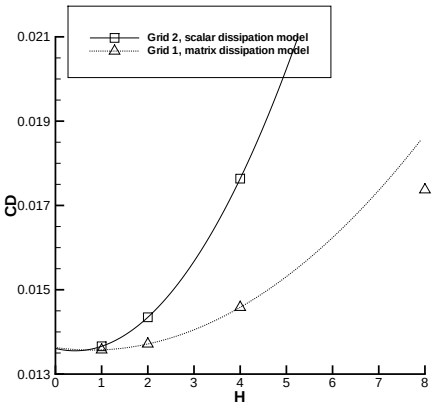

Figure 7: Drag extrapolation for wind tunnel configuration at tunnel Reynolds number

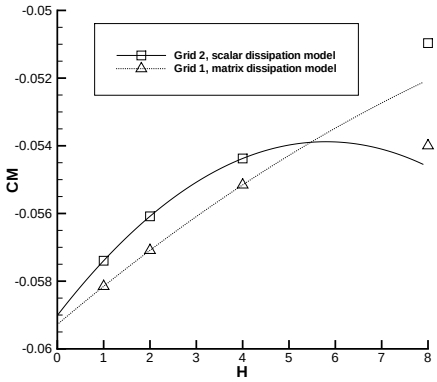

Figure 8: Pitching moment extrapolation for wind tunnel configuration at tunnel Reynolds number

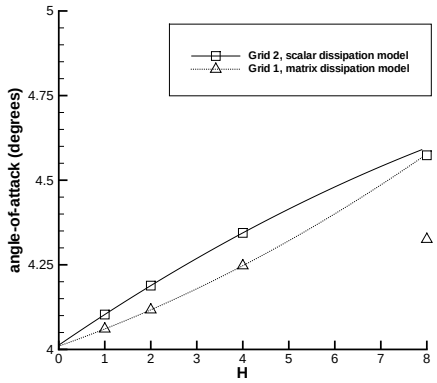

Figure 9: Angle-of-attack extrapolation for wind tunnel configuration at tunnel Reynolds number

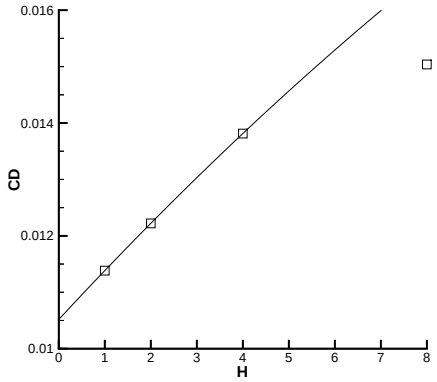

Figure 10: Drag extrapolation for wind tunnel configuration at flight Reynolds number

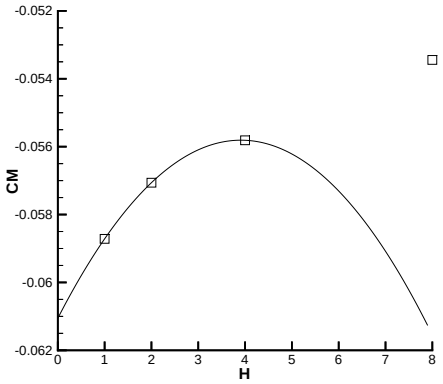

Figure 11: Pitching moment extrapolation for wind tunnel configuration at flight Reynolds number

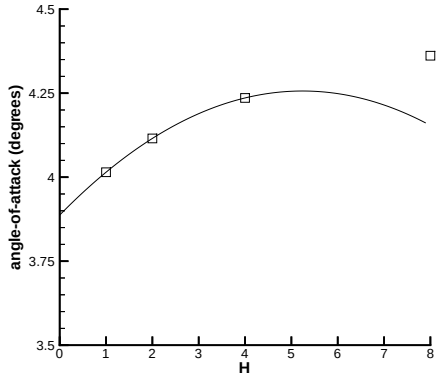

Figure 12: Angle-of-attack extrapolation for wind tunnel configuration at flight Reynolds number

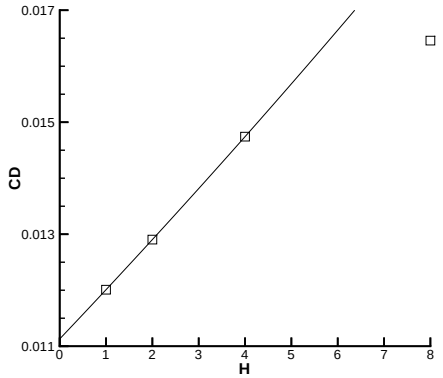

Figure 13: Drag extrapolation for flight configuration at flight Reynolds number

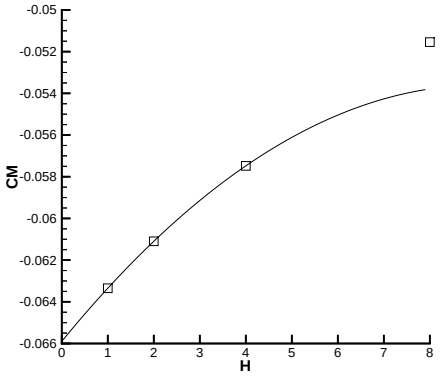

Figure 14: Pitching moment extrapolation for flight configuration at flight Reynolds number

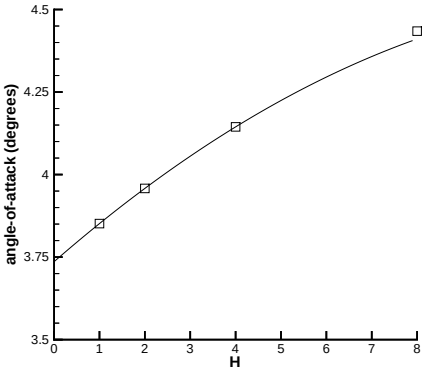

Figure 15: Angle-of-attack extrapolation for flight configuration at flight Reynolds number

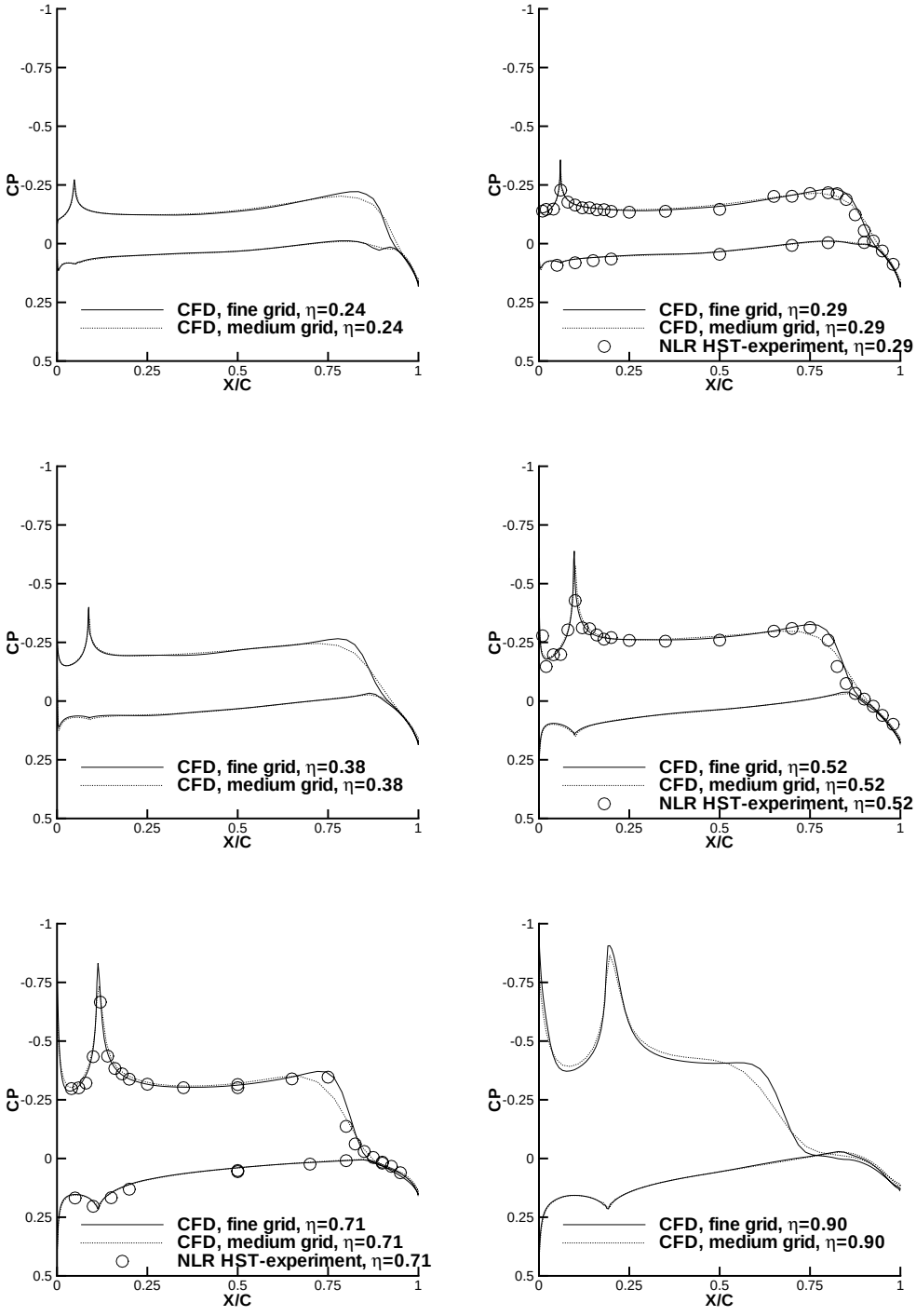

Figure 16: Comparison of computed and measured pressure distributions at selected span stations: design condition at tunnel Reynolds number

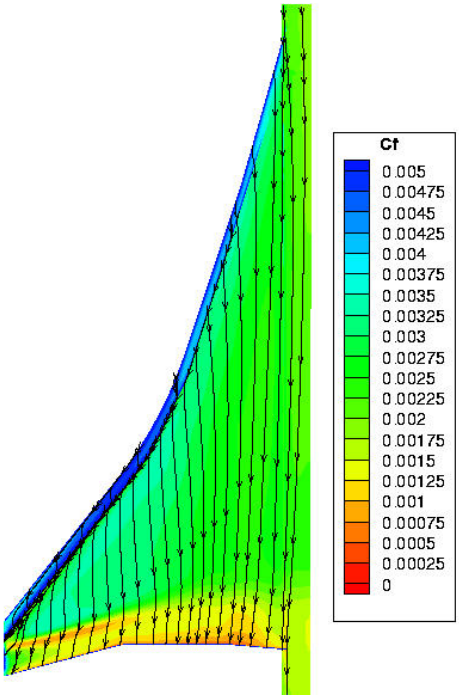

Figure 17a: Wing upper side skin friction and limiting streamlines (design condition at tunnel Reynolds number)

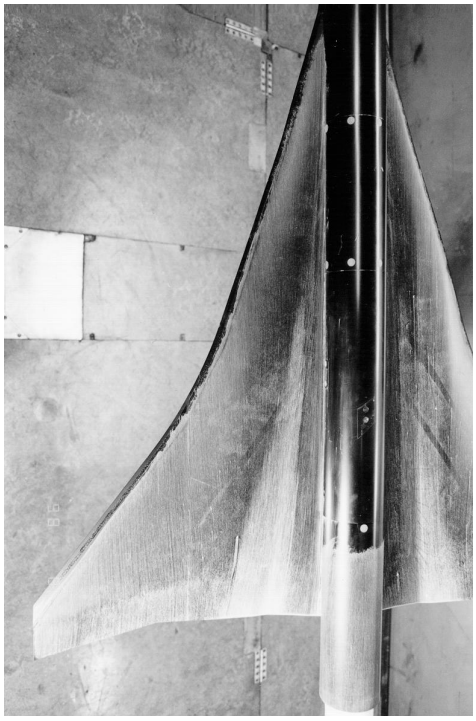

Figure 18a: Wing upper side oil flow pattern at the transonic design condition

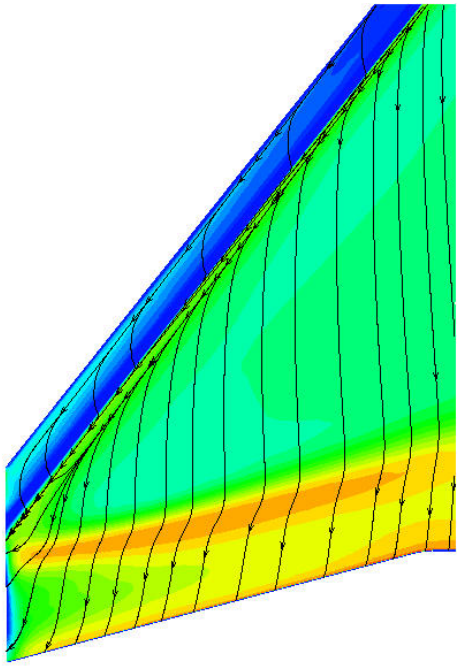

Figure 17b: Detailed view of outer wing upper side skin friction and limiting streamlines

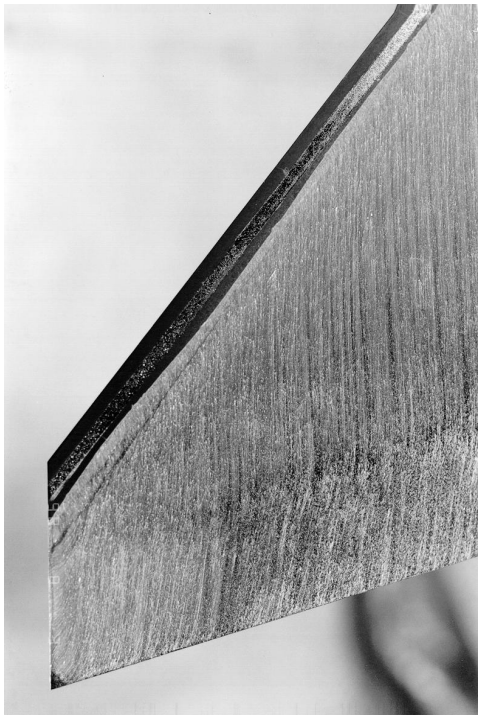

Figure 18b: Detailed view of outer wing upper side oil flow pattern at the transonic design condition

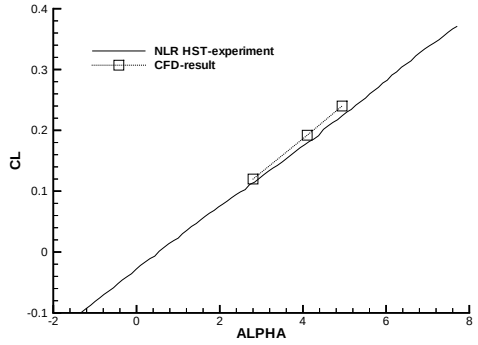

Figure 19: Lift curve comparison for wind tunnel configuration at tunnel Reynolds number: CFD versus experiment

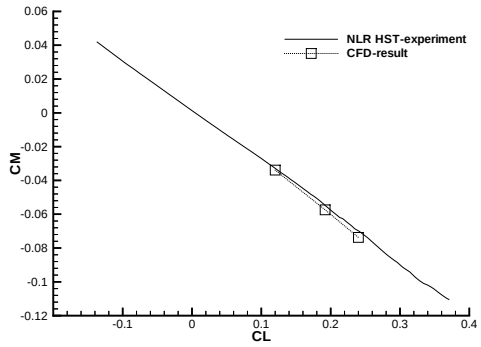

Figure 20: Pitching moment comparison for wind tunnel configuration at tunnel Reynolds number: CFD versus experiment

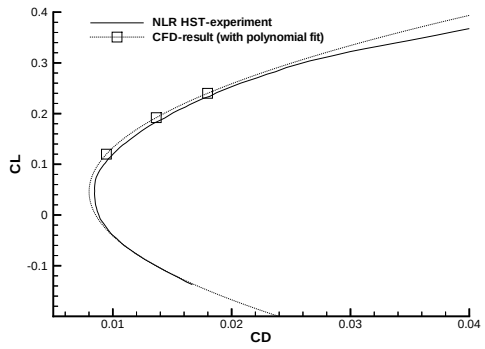

Figure 21: Drag polar comparison for wind tunnel configuration at tunnel Reynolds number: CFD versus experiment

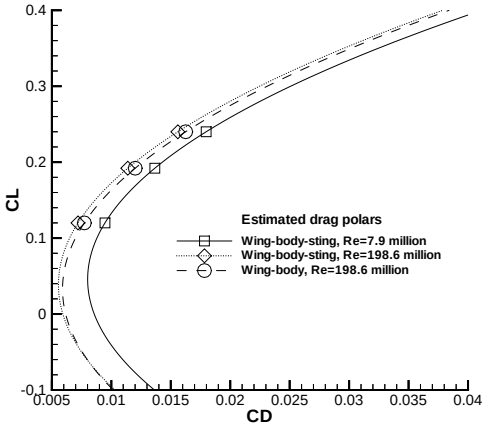

Figure 22: Comparison of estimated drag polars for both configurations at different Reynolds numbers

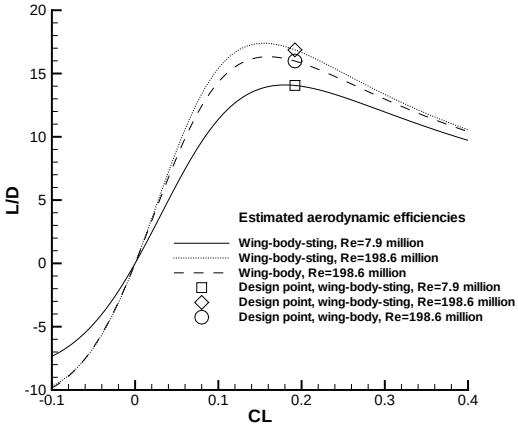

Figure 23: Comparison of estimated aerodynamic efficiencies versus lift coefficient based on estimated drag polars for both configurations at different Reynolds numbers

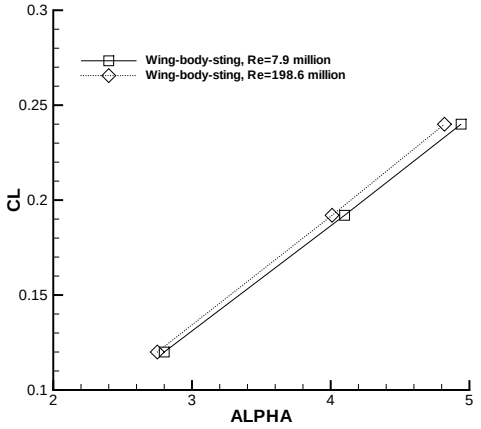

Figure 24: Computed Reynolds number effect on lift curve for wind tunnel configuration

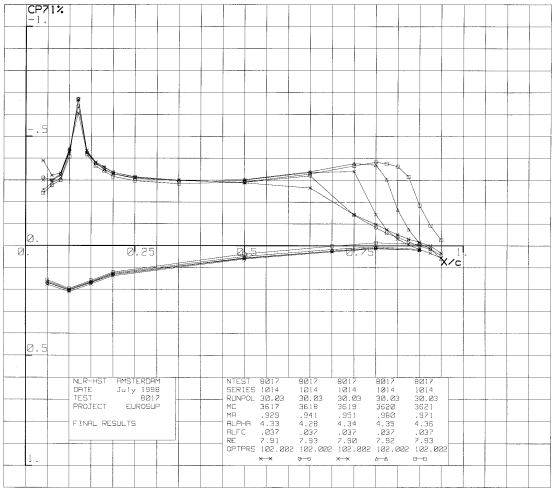

Figure 26: Experimentally observed sensitivity of shock position due to small Mach number increments around the design condition (ΔM=0.01)

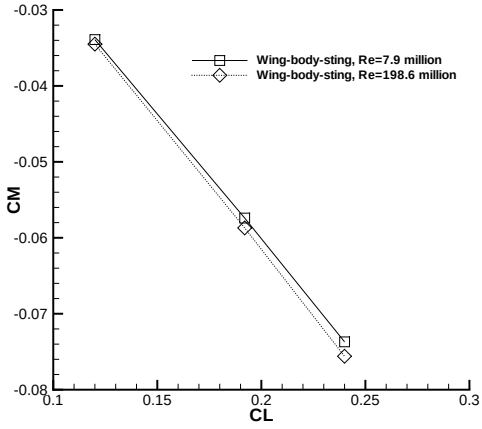

Figure 25: Computed Reynolds number effect on pitching moment for wind tunnel configuration

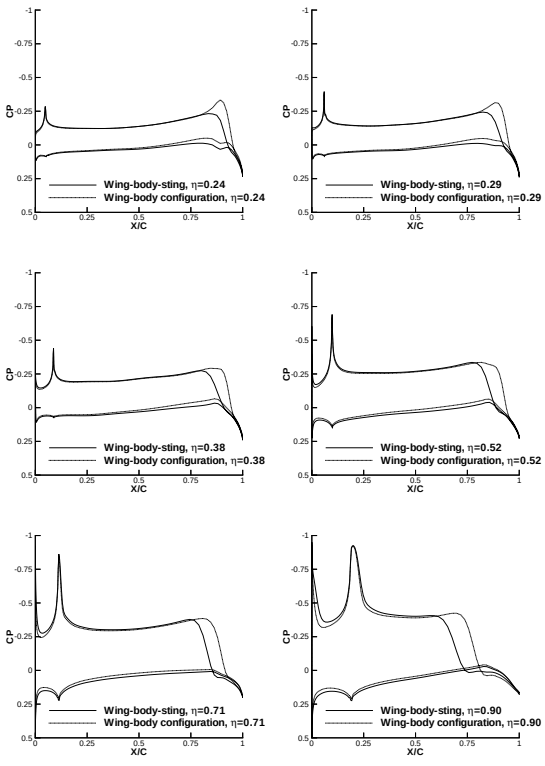

Figure 27: Comparison of pressure distribution at selected span stations for both configurations at flight Reynolds number

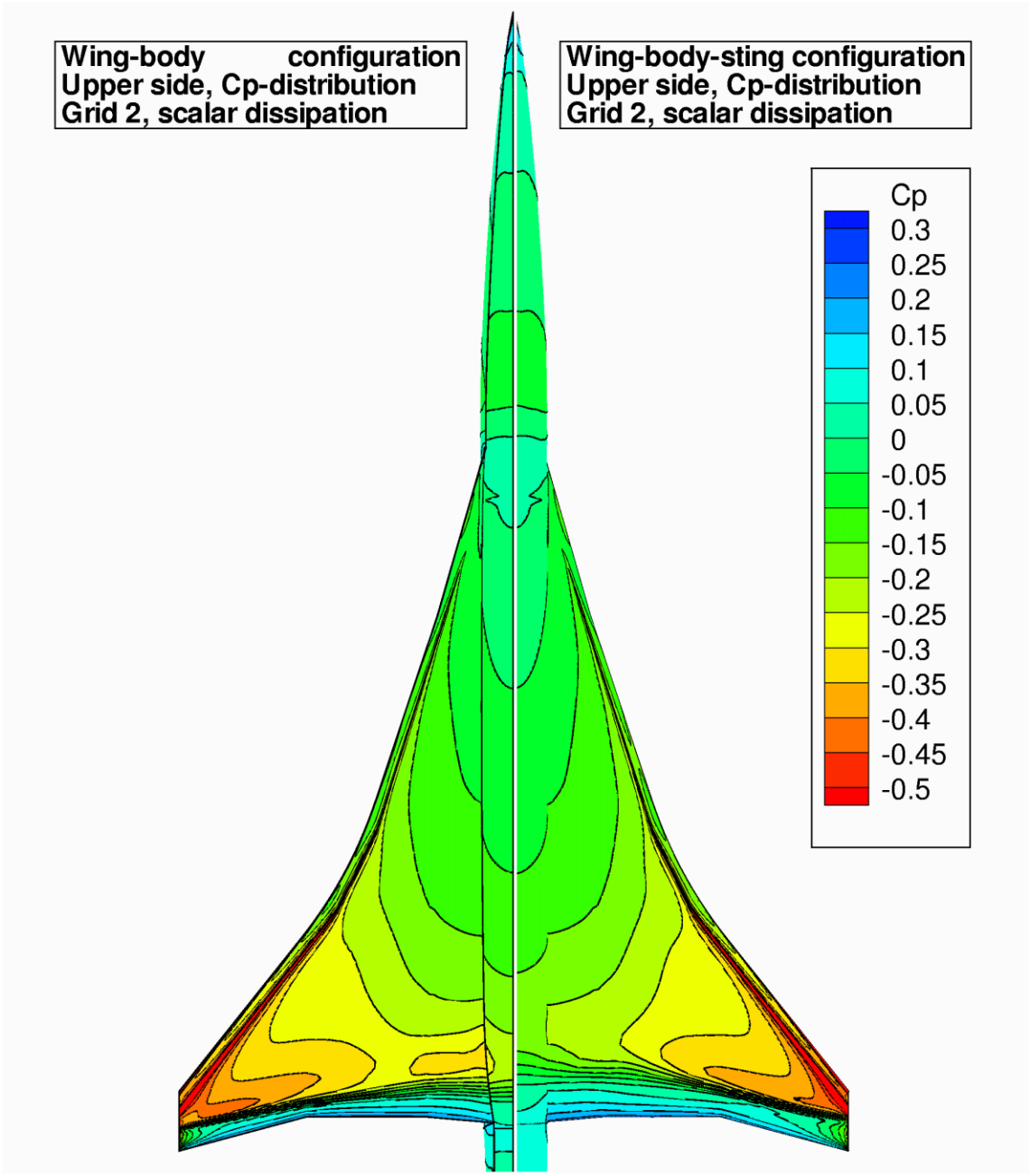

Figure 28: Comparison of upper side pressure distribution for wind tunnel (right) and flight (left) configuration at the transonic design condition (flight Reynolds number)